

# HIGH-FIDELITY MULTIDISCIPLINARY MANEUVER SIMULATIONS OF THE FALCON 2000LX ISTAR

Martin Bauer<sup>1</sup>, Johan Feldwisch<sup>2</sup>

<sup>1</sup>German Aerospace Center DLR, Institute of Aerodynamics and Flow Technology, Lilienthalplatz 7,  
38108, Braunschweig, Germany, Ma.Bauer@dlr.de

<sup>2</sup>German Aerospace Center DLR, Institute of Aeroelasticity, Bunsenstr a e 10, 37073, G ttingen,  
Germany, Johan.Feldwisch@dlr.de

**Keywords:** Maneuver simulation, Virtual flight testing, Simulation based certification, Simulation validation.

**Abstract:** This paper presents high-fidelity multidisciplinary maneuver simulations of the DLR research aircraft Dassault Falcon 2000LX ISTAR. These simulations are computed using the multidisciplinary process chains FSAerOpt and UltraFLoads for the DLR research project HighFly (High-Speed Inflight Validation). The goal of this project is the validation of simulation models for virtual flight testing with data measured on the ISTAR aircraft. The paper describes the individual ISTAR models and analyses: CAD geometry, CFD (DLR TAU-Code), control surface deflection modeling, CSM (MLS Nastran), aircraft mass distribution, and engine. The paper gives also a short overview of some UltraFLoads simulation processes such as CFD-CSM coupling, trim analysis, and dynamic maneuver simulation. The results of steady-state trimmed CFD-CSM coupled simulations and unsteady open-loop free-flying elastic maneuver simulations (pull-up, push-down, bank-to-bank) in clean configuration are presented. The first comparisons of the numerical simulations with the experimental data are also shown.

## 1 INTRODUCTION

### 1.1 Motivation for virtual flight testing

The central goal in current aviation research and development is increasing the efficiency of aircraft and reducing their impacts on the climate. Important to achieving these goals is the ability to accurately and quickly analyse the characteristics of the aircraft such as flight performance, flight loads, aeroelastic phenomena, flight control, and stability with numerical simulation methods. They do not have to be used only at the early stages of development, but also at later stages to create an aircraft digital twin for virtual flight testing and simulation-based certification [1]. In the future, virtual flight tests could at least partially replace real certification flight tests that are associated with high costs and time demands. With virtual flight tests, problems or errors in the aircraft design can also be detected at an early stage. Extensive verification and validation activities must first be carried out to confirm a sufficient accuracy and level of fidelity of the numerical simulations. This creates the necessary confidence and acceptance for using these methods for simulation-based certification by the certification authorities and the aircraft

manufacturers [2]. Virtual flight tests should then enable faster and more cost-effective progress of new technologies towards climate-neutral air transport and reduce development risks.

### 1.2 Challenges of transport aircraft maneuver simulations

Due to lightweight structures, the high aspect ratio wings on modern transport aircraft (e.g., Airbus A350 or Boeing 787) are highly flexible, which leads to a strong interaction between the flow and the wing deformation. This means an interaction between the aerodynamic, elastic, and inertial forces, as described by the Collar aeroelastic triangle [3] depicted in Figure 1.

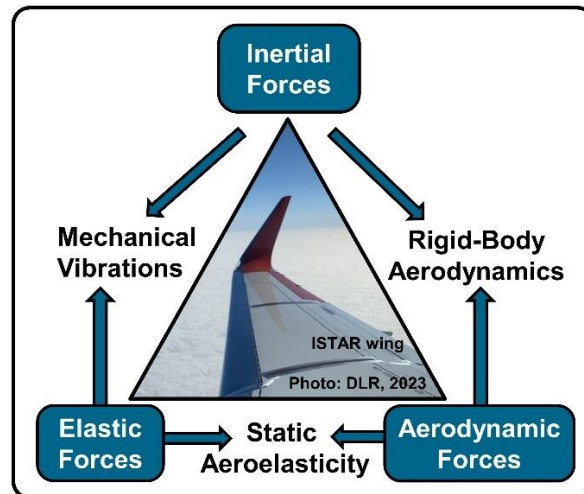


Figure 1: Collar's aeroelastic triangle [3].

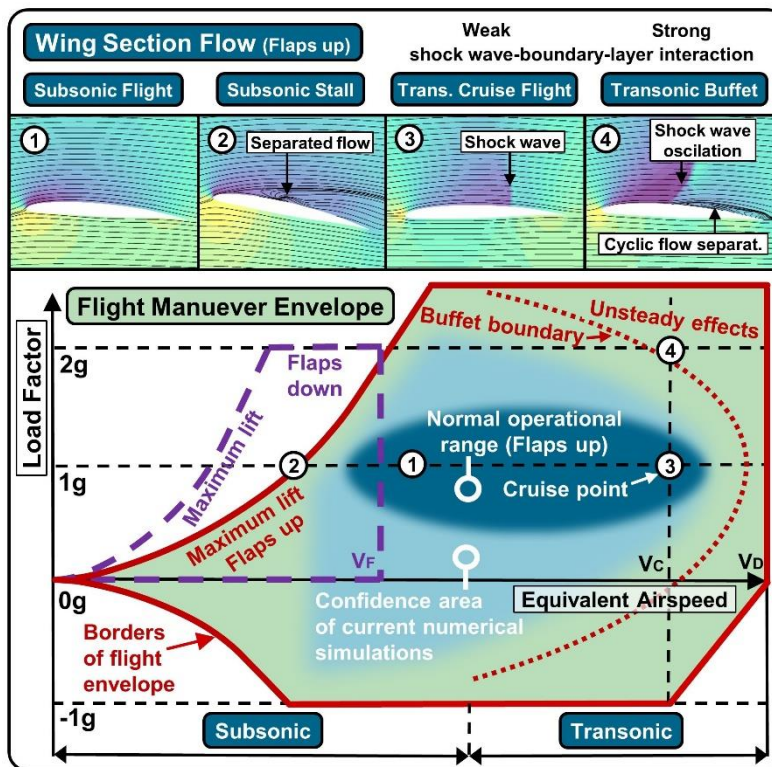


Figure 2: Transport aircraft flight maneuver envelope (schematic depiction).

The calculation of aerodynamic loads in the transonic regime is very challenging due to strong nonlinear phenomena such as shock wave-boundary-layer interaction, which can lead to fast oscillation of the shock wave (buffet) on the wing at higher transonic Mach numbers and angles of attack (Figure 2, point 4). In addition to the shape of the elastically deformed aircraft, the aerodynamic loads during maneuver are directly coupled to the local inflow velocities relative to aircraft (magnitude and direction). This requires the inclusion of the aircraft flight mechanics discipline that describes the translational and rotational 6DoF (six degrees of freedom) motion of the free-flying aircraft. Elastic motion of the aircraft, especially on the outer part of the wings, also induces local flow velocities, which must be considered in the aerodynamic calculation. The same effect is also induced by dynamic flight control surface deflections. All this makes the simulations of the dynamic flight maneuvers of free-flying elastic aircraft in the transonic regime, especially at the borders of the flight envelope, very complex. Multidisciplinary analysis (aerodynamics, structural dynamics, and flight dynamics) and unsteady nonlinear high-fidelity solver for aerodynamic analysis (such as URANS) are required. Due to the direct coupling among disciplines, an inaccurate calculation of one discipline, due to insufficient physical modelling for example, leads to incorrect overall results, even if the other numerical models are highly accurate.

### 1.3 Current status of maneuver simulations and DLR project HighFly

Continuous developments in high-performance parallel computing makes it possible to investigate more detailed aircraft geometries described by Computer-Aided Design models (CAD) and to use high-fidelity numerical physical models such as Computational Fluid Dynamics (CFD), Computational Structural Mechanics (CSM), thermodynamic engine models, and flight mechanics models. These models can then be combined into one multidisciplinary multi-physics process chain. They are becoming increasingly important in aircraft research and development. They can be used in the analysis, design, and optimization of almost all flight cases, for example:

- Performance calculation (cruise, climb, takeoff, landing, flight with engine failure)
- Technology assessment (load alleviation, new aircraft configurations and propulsion systems)
- Load calculation (flight maneuver, gust, turbulence)
- Flight mechanics (static and dynamic stability, controllability, handling quality, flight control surface design)
- Aeroelasticity (flutter, buffeting, divergence, control reversal)
- Ice on aircraft surface analysis
- Flying through wake vortexes
- Creation of flight mechanics models for flight simulators

Also, for new future aircraft configurations, where the experience of engineers and scientists and well-calibrated lower fidelity methods are lacking, high-fidelity methods based on accurate physical models are necessary.

The important task before applying these methods reliably in practice, both in research and industry, is validation, i.e., comparing numerical results with experimental data. This is the goal of the DLR research project HighFly (High-Speed Inflight Validation), running from 2018 to 2023 [4]. In this project, the new DLR research aircraft Dassault Falcon 2000LX ISTAR [5], shown in Figure 3, was used for scientific research for the first time. Falcon 2000LX is a French super mid-sized business jet with the following characteristics: certified up to 19 PAX, max. range=7400 km,

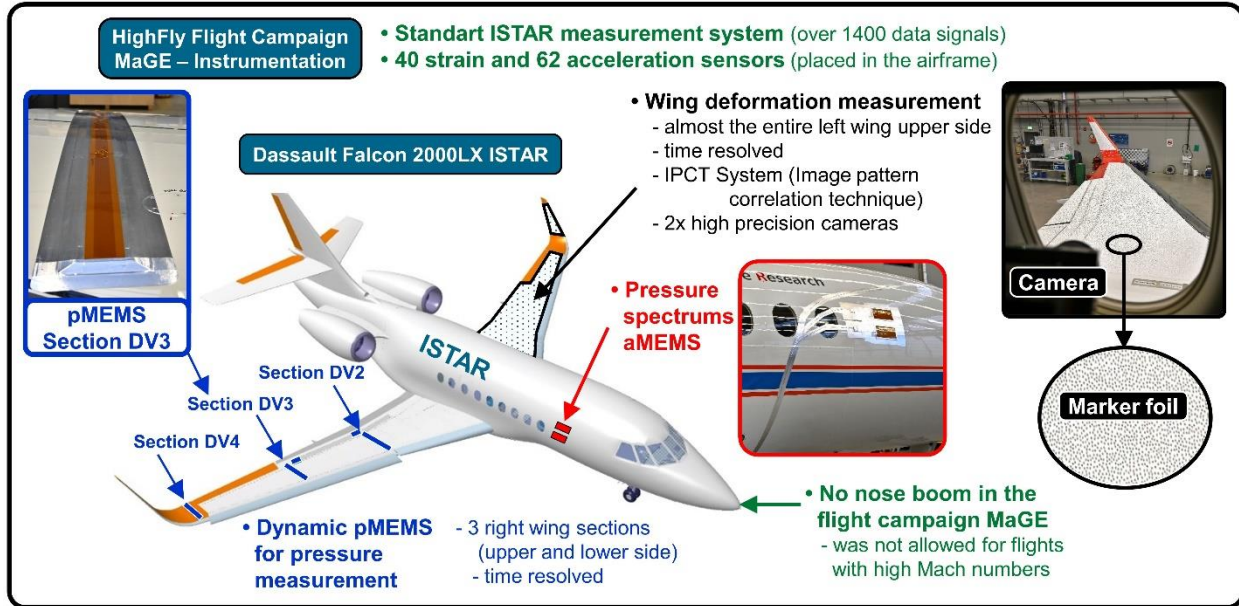


Figure 3: HighFly flight campaign MaGE – ISTAR instrumentation.

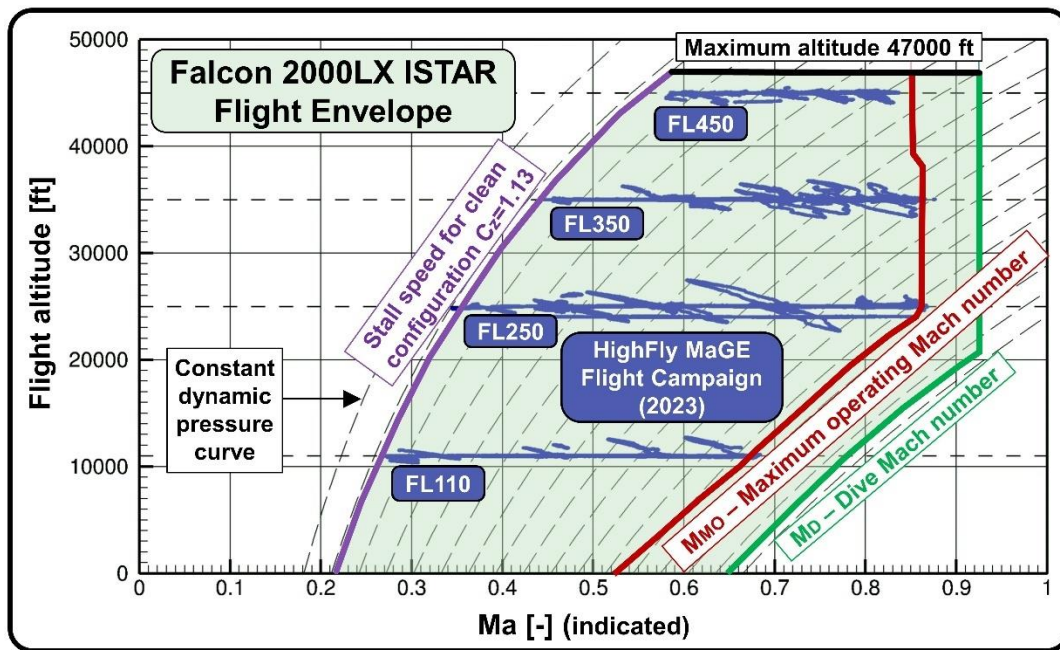


Figure 4: HighFly flight campaign MaGE in the ISTAR flight envelope.

MTOW=19142 kg, MMO=0.85/0.862 and service ceiling=47000 ft. Its wings are not as elastic compared to modern transport aircraft wings, but due to the high aircraft agility, highly dynamic maneuvers are possible. New advanced measurement technologies were developed and evaluated in several ground and flight measurement campaigns with ISTAR in the project HighFly [6, 7]. Figure 3 presents measurement instruments for the HighFly flight campaign MaGE (maneuvers at the border of the envelope), including a high-precision wing section pressure measurement based on MEMS [8] and a wing deformation measurement based on IPCT [9]. The MaGE flight campaign, performed in 2023, contained over 30 flight hours and over 500 maneuvers: trimmed

level turns, pull-up and push-down maneuvers, bank-to-bank maneuvers with different roll speeds, level accelerations and decelerations, maneuvers with several elevator pulses as 13221 or single aileron pulse, and steady heading side slips, covering the complete flight range in clean configuration (Figure 4). From a related flight test campaign of another project, data of stall maneuvers at low speeds in clean configuration are also available for validation. The combination of the ISTAR instrumentation is unique worldwide. The pressure sensors pMEMS and the acoustic sensors aMEMS were used in the transonic speed range under real flight conditions for the first time at DLR. With this high-quality flight test data, the validation of simulation models for virtual flight testing and the quantification of numerical uncertainties is carried out. Especially valuable here are the flight measurement data outside the normal operational range close to the edges of the flight envelope. As displayed in Figure 2, numerical simulations are still not considered reliable in these regions. Currently used (U)RANS CFD methods are not able to handle separated flows with sufficient reliability. The ongoing validation will show the accuracy and applicability limits of the current high-fidelity multidisciplinary simulations that are presented in this paper. Furthermore, it will provide best-practice approaches and show efficiency, robustness, and procedural gaps.

There is a growing interest in the aviation industry in using more reliable numerical simulations instead of the low-fidelity methods based on the potential theory for computation of the unsteady off-design conditions such as unsteady flight loads (gust and maneuvers). High-fidelity CFD analysis (such as RANS) is often used only for static aeroelastic simulations, but not for dynamic aeroelastic simulations coupled with a dynamic structural solver and flight dynamics model, due to the high computational time. In the future, the off-design accuracy of numerical models will be crucial in the simulation-based certification, where aircraft will be pushed to their flight performance and safety limits during virtual flight tests.

#### **1.4 Content of the paper**

For the ISTAR maneuver simulations in the clean cruise configuration, the multidisciplinary process chains FSAerOpt and UltraFLoads are used. FSAerOpt is used for steady-state trim cases, and UltraFLoads for steady-state trim cases and dynamic maneuvers. In the next section these two process chains are briefly introduced. After that, the individual numerical models and analyses of ISTAR are described (CAD, CFD, control surface deflection, CSM, mass distribution and engine). Afterwards, UltraFLoads processes, which connect different numerical models, are introduced (CFD-CSM coupling, trim analysis, and dynamic maneuver simulation). Finally, the result section shows maneuver simulations such as steady-state CFD-CSM coupled simulation of different trimmed horizontal flights, and simulation of several dynamic maneuvers, including the first comparisons with the experimental data.

This paper serves as a presentation and demonstration of the maneuver simulation capabilities and methods being developed at DLR. The complete results of the HighFly maneuver simulation validation activities will be introduced in future papers. Some parts of the results presented in this paper were presented at the DLRK 2023 conference in Stuttgart [10].

## 2 MANEUVER SIMULATION PROCESS CHAINS, NUMERICAL MODELS, AND ANALYSES OF ISTAR

### 2.1 Maneuver simulation process chains

#### 2.1.1 *Process chain FSAerOpt*

The process chain FSAerOpt was developed in the CAS department (Center for Computer Applications in AeroSpace) of the DLR Institute for Aerodynamics and Flow Technology in Braunschweig and was created mainly for multidisciplinary design optimization (MDO), but can be used also for multidisciplinary analysis (MDA). FSAerOpt performs steady-state trimmed CFD-CSM coupled simulations in the FlowSimulator framework, jointly developed by DLR, Airbus and ONERA [11, 12]. The FlowSimulator suite is a software integration framework for highly parallel CFD-based multidisciplinary simulations on HPC. FSAerOpt uses MSC Nastran [13] as a structure solver and DLR TAU-code [14] as a flow solver. The engine thrust can be considered either by force vector or as CFD boundary conditions. The latter can be coupled with a thermodynamic engine model. The aircraft is trimmed by adjusting the angle of attack, engine thrust, and elevator deflection or horizontal stabilizer rotation. The process chain FSAerOpt can only calculate symmetrical steady-state flight cases and only the half CFD geometry is used in simulations. More information about FSAerOpt can be found in [15, 16].

#### 2.1.2 *Process chain UltraFLoads (UFL)*

The process chain UltraFLoads has been developed in the Loads Analysis and Aeroelastic Design department of the DLR Institute for Aeroelasticity in Göttingen. It is a Python-based MDA simulation software focusing on aeroelastic applications with high-fidelity methods like CFD. It utilizes data objects and plugins of the FlowSimulator and its DataManager [11, 12]. UltraFLoads provides an outer scenario layer to the FlowSimulator eco-system. In addition to the steady trim cases, dynamic maneuvers can be simulated with an implementation of the unsteady structural modal analysis and the flight mechanics calculation (rigid body motion). UltraFLoads processes, such as CFD-CSM coupling, trim simulation, and dynamic maneuver simulation are briefly described in section 2.5. More detailed information about the architecture and the capabilities of UltraFLoads can be found in [17, 18], and two applications are presented in [19, 20].

### 2.2 CFD analysis

#### 2.2.1 *ISTAR CAD model for CFD*

The base of the ISTAR geometry description was the CATIA V5 CAD model [21] of Falcon 2000LX delivered by Dassault Aviation. This was corrected by the aircraft optical measurements in the HighFly project. Then a complete ISTAR geometric digital mock-up was created, from which the external surface geometry for CFD simulations was derived. The CAD model in clean configuration (retracted flaps and landing gear) in unloaded shape contains wings, fuselage, horizontal tail parts (HTP), vertical tail part (VTP), engine nacelles, pylons, and flap track fairings (FTF), see Figure 5. The engine geometry has one inlet surface with a spinner and one outlet surface, where the boundary conditions are set in CFD. The CAD model does not include small details such as antennas, sensors, lights, aircraft system inlets and outlets, and enhanced flight vision camera fairing on the nose upper side. The CAD geometry has a smooth surface: no rivets, embossing, and gabs, except for the ailerons. Figure 6 shows a modified wing geometry with pMEMS belts (blue color) for surface pressure measurements.



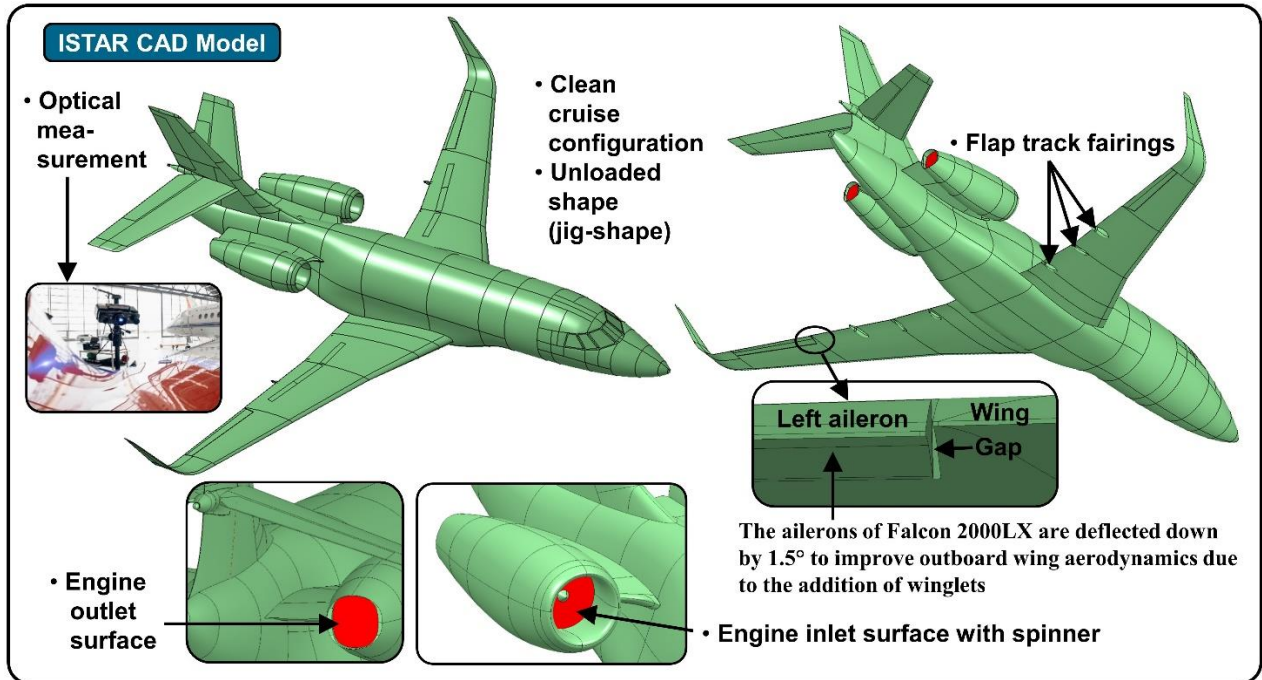


Figure 5: CAD geometry of Falcon 2000LX ISTAR for CFD.

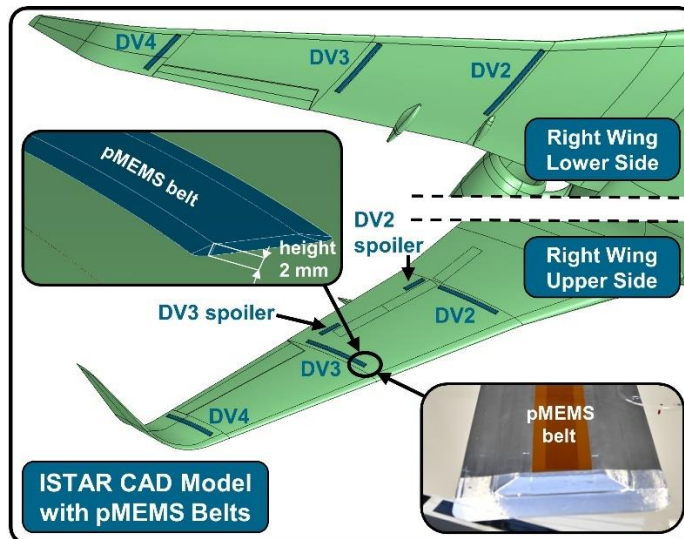


Figure 6: ISTAR CAD wing geometry with pMEMS belts.

### 2.2.2 ISTAR CFD meshes

A set of CFD meshes were created using the SOLAR mesh generator [22] and the ANSA mesh generator [23]. In both cases, it is an unstructured mixed-element type, with prism layers of mostly hexahedral cells in the surface vicinity for a better resolution of the boundary layer flow. The number of grid points in the generated CFD meshes range from 7 to 60 million in half configuration. Figure 7 shows an ANSA mesh with 25 million grid points in half configuration with hexahedral cells in the outer flow field. A mesh refinement in the aircraft downwash region (transparent blue boxes) and around the wing for better resolution of the shock wave is visible. Some mesh sensitivity studies were performed but are not shown here. In the FSAerOpt

simulations presented, the half CFD configuration with a symmetry plane is always calculated. In the UltraFLoads simulations, the full CFD configuration is always used, which is created by mirroring the half configuration.

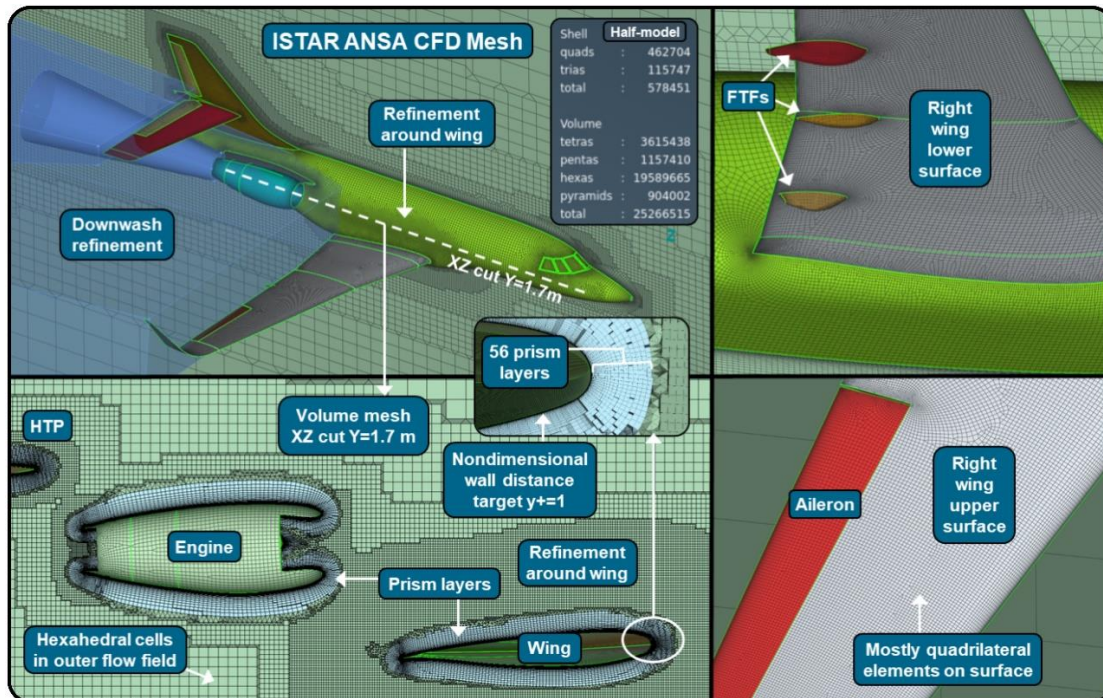


Figure 7: ISTAR ANSA CFD mesh.

### 2.2.3 ISTAR CFD TAU simulations

The flow analysis is calculated with the high-fidelity DLR TAU-Code [14], developed at the DLR Institute of Aerodynamics and Flow Technology. The DLR TAU-Code is highly validated CFD solver, with over 25 years of development and used in many academic and industrial projects. It is a parallel CFD cell-vertex finite volume software package and can solve the steady and unsteady Reynolds-averaged Navier-Stokes equations (RANS) on unstructured meshes. The compressible and viscous flow around the ISTAR geometry is calculated in a fully turbulent regime, which is assumed due to the Falcon 2000LX turbulent swept wing and high Reynolds numbers in cruise flight. The RANS models are considered as a good compromise between accuracy and computation time. In most cases, the negative extension of the Spalart-Allmaras (SA-neg) one-equation turbulence model [24] is used. In a later presented parameter variation study, simulations with the two-equation models  $k$ - $\omega$ -SST-1994 [25] and SST- $k$ - $g$  [26] are computed as well. It is also planned to use the Reynolds-stress turbulence model (RSM) at a later stage. More accurate CFD techniques such as LES or DES, which would be very beneficial, for example, in investigating the shock wave-boundary-layer interaction, are still unattainable for complex configurations such as ISTAR in time-resolved elastic maneuver simulations. In most cases, the second-order spatial discretization based on the scalar-dissipative central convection scheme and Green-Gaussian gradients for the viscous flux is used. The implicit backward-Euler time stepping scheme is chosen as a relaxation method. The corresponding systems of linear equations are solved by symmetric forward-backward Gauss-Seidel iterations (LUSGS). URANS calculations use the dual-time stepping and to save computational time, a Cauchy convergence criterion is applied.



In the UltraFLoads simulations the DLR TAU-Code considers grid velocities due to mesh deformation and rigid body motion (ALE-formulation). The mesh deformation results from the control surface deflections, HTP rotation, and structural deformation. Instead of prescribing the flow velocity boundary condition at the CFD far-field surface, the grid velocities are defined by the rigid body motion of the whole CFD domain, enabling dynamic maneuver simulations. This motion is described by a geodetic position, Euler (position) angles, and translational and angular velocities (12 variables). The CFD boundary conditions of the power engine are described in section 2.4.

It is planned to replace the DLR TAU-Code in the future with the next-generation CFD solver CODA [27], jointly developed by DLR, Airbus, and ONERA.

### 2.2.4 ISTAR flight control surface modelling in CFD

Due to the trimming and maneuver simulations, it is necessary to model the deflection or rotation of the ISTAR control surfaces in the CFD mesh. For the ISTAR simulations with UltraFLoads, all primary flight control surfaces are modeled (Figure 8) using FlowSimulator plugins [28].

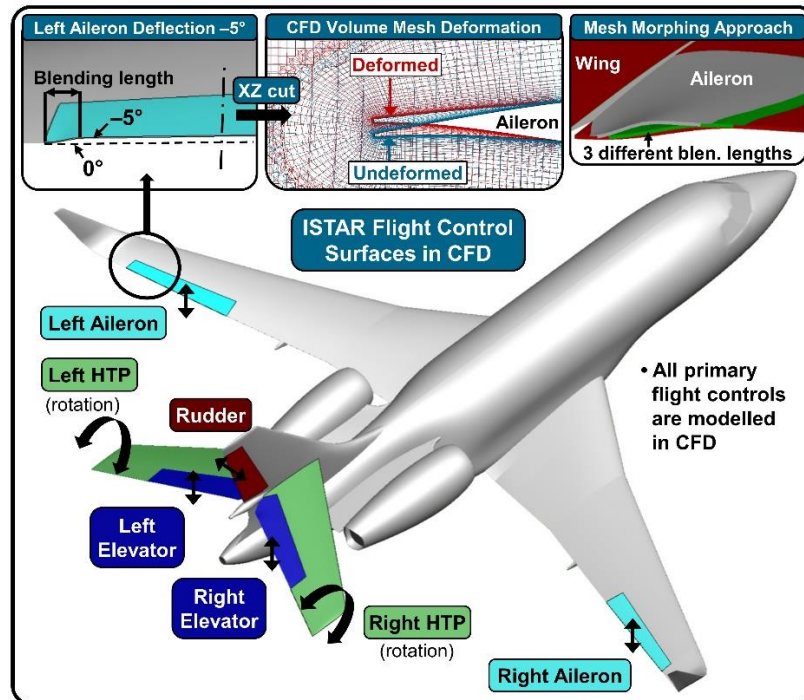


Figure 8: ISTAR flight control surface modelling in CFD.

A simplified control surface deflection with user-defined blending areas (mesh morphing approach) is used for both ailerons, elevators, and the rudder. This provides a smooth transition between a deflected control surface and a remaining undeflected area and gives a robust volume mesh deformation but causes a modelling error. The trimmable horizontal stabilizer (HTP) is rotated. After the calculation of control surface displacement fields, the CFD volume mesh is deformed with the Radial Basis Function (RBF) mesh deformation method of FlowSimulator [29]. This interpolation function gives a gradual decline of mesh node deflections from the deflected surface into the volume mesh. Different deformation surface groups can be defined: free for

deformation in all three dimensions, fixed for no deformation, and no normal movement. The latter condition is used by the HTP rotation for the surrounding VTP surfaces to avoid negative mesh cells. In the case of negative mesh cells, a mesh repair step can be locally applied with the linear elasticity method. The CFD-CSM coupling is based on Radial Basis Functions as well.

## 2.3 CSM analysis

### 2.3.1 ISTAR CSM model and calculation

Aeroelastic simulations require calculations of the structural deformation. The commercial finite element (FE) software MSC NASTRAN [13] is used. An FE NASTRAN structural model of the ISTAR aircraft with 24863 nodes provided by the DLR Institute of Aeroelasticity in Göttingen is displayed in Figure 9.

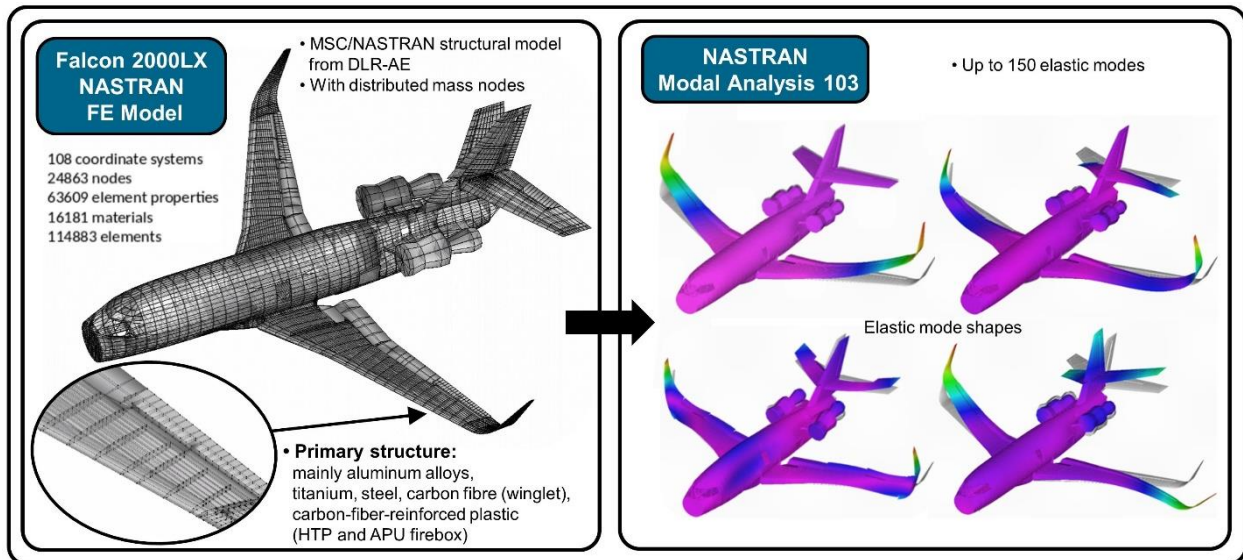


Figure 9: ISTAR CSM model.

This model of the mainly aluminum Falcon 2000LX consists of the load-carrying structure (fuselage, wings, HTP, VTP, engines and pylons) represented by elements like spars, ribs, stringers and skins. The structural model does not contain any damping. In the process chain FSAerOpt, the NASTRAN linear static analysis (SOL 101) is calculated in the loop with the FE model. For this work, UltraFLoads uses the modal approach ([18] section 3.4) with the modal shapes and corresponding natural frequencies that are computed from the FE model with NASTRAN free-free modal analysis (SOL 103). Up to 150 elastic modes in the range of natural frequencies up to 60Hz are selected to approximate the structural deformation (reduced order model). Using linear structural methods for this aircraft is reasonable, as the aircraft is stiff and the deformation stays within the linear range.

### 2.3.2 ISTAR mass distribution

The aircraft masses are not determined by material densities of individual elements in the FE model but by distributed mass nodes, shown in Figure 10 (airframe, fuel, and cabin masses). The model mass distribution can be adjusted for different aircraft mass configurations by scaling mass nodes in the cabin and 10 individual fuel tanks with a created Python tool.

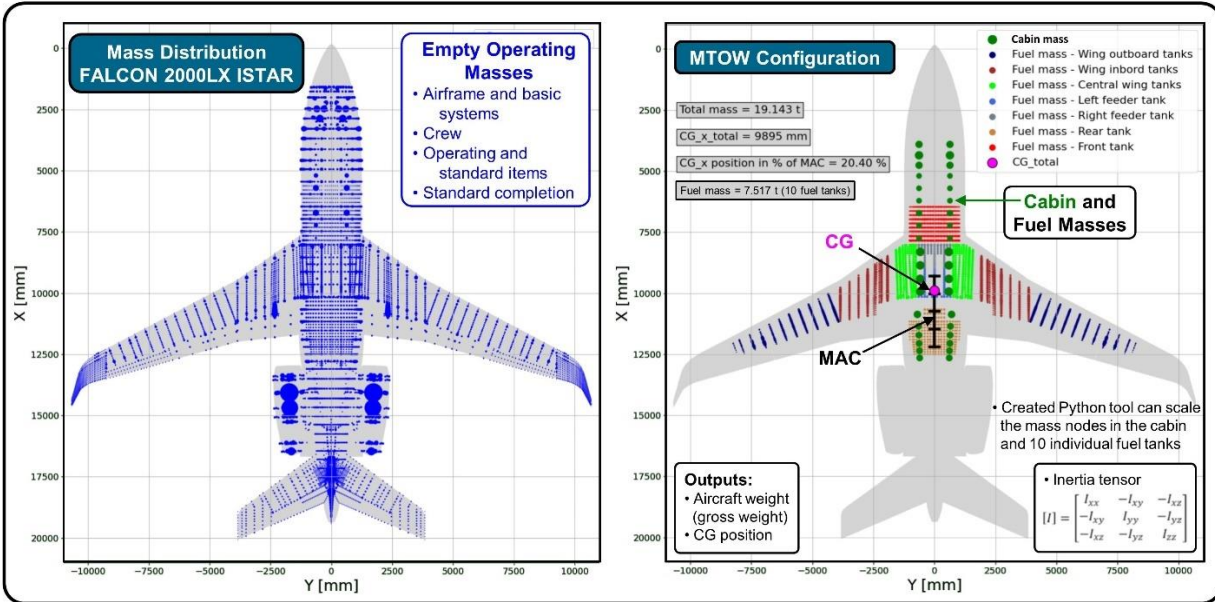


Figure 10: ISTAR mass distribution in NASTRAN FE model.

## 2.4 ISTAR engine model

In the process chain FSAerOpt, it is possible to couple TAU flow simulation with a DLRp2 thermodynamic performance model [30] (DLR Performance Program) of the ISTAR engines (PW308C) delivered from the DLR Institute of Propulsion Technology in Berlin. For a specified Mach number, altitude, and engine thrust, this model calculates, among other variables, the thermodynamic flow variables for the inlet and outlet surface of the powered engine in the TAU CFD domain (Figure 11).

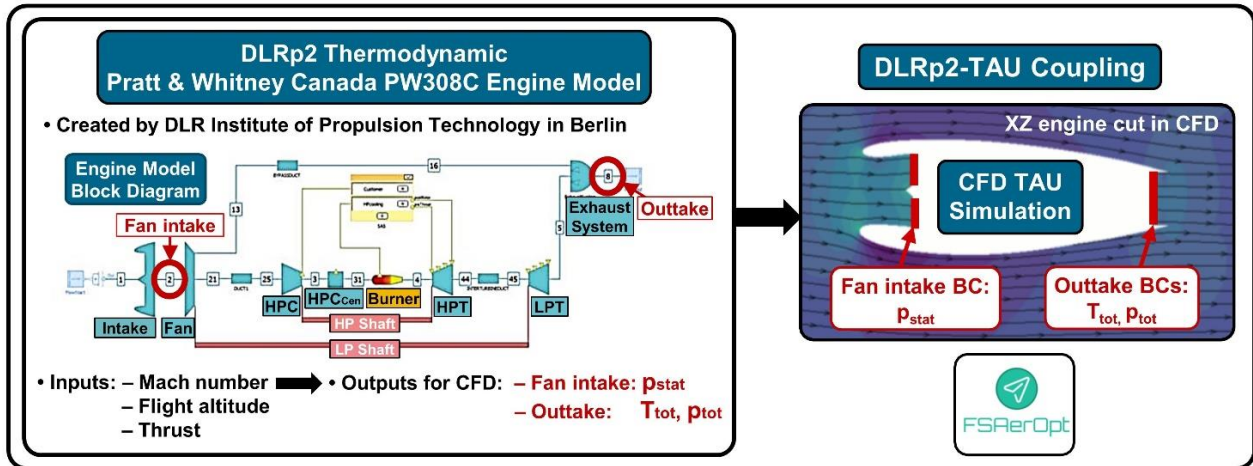


Figure 11: TAU coupling with DLRp2 engine model of ISTAR in FSAerOpt.

In the process chain UltraFLoads, the TAU engine inlet and outlet flow variables are based on the FSAerOpt results and are kept constant during the UltraFLoads trim analysis, where an artificial force vector can be applied.

## 2.5 Process of dynamic maneuver simulation in UltraFLoads

In the previous sections, individual numerical models and analyses of the ISTAR aircraft were described in isolation. In this section, their connections in different UltraFLoads processes are briefly presented.

The left part of Figure 12 schematically shows the UltraFLoads process of the steady-state CFD-CSM coupled simulation. The aeroelastic coupling starts with the aerodynamic CFD analysis (TAU). The aerodynamic loads are then interpolated from the CFD mesh to the CSM mesh and serve as boundary conditions for the structural analysis. The resulting structural deformations are interpolated to the CFD surface mesh and then propagated to the CFD volume mesh (RBF mesh deformation) and the next iteration of the aeroelastic coupling begins. This iterative process is terminated when the user-defined criteria are met.

The right part of Figure 12 schematically displays the trim simulation process in which the angle of attack (AoA), the elevator deflection (or HTP rotation), and the thrust vector are changed until the translational acceleration X and Z and the pitch rotation acceleration Y are close to zero according to user-defined criteria. This flight condition then represents unaccelerated trimmed 1 g horizontal flight.

FSAerOpt processes of steady-state CFD-CSM coupled simulation and trimming, which are not shown here, use similar methods as UltraFLoads, but there are some differences, for example, linear static analysis instead of linear modal analysis. Information about FSAerOpt processes can be found in [15, 16].

Figure 13 schematically shows an overall UltraFLoads workflow of simulation of the open-loop flight dynamic response to a flight control surface deflection input for a flexible, free-flying aircraft. The first step is to trim the steady-state, free-flying, elastic aircraft. The dynamic maneuver simulation (second step) with forced motion of the control surface deflections starts from the trimmed state. The aircraft rigid body motion (flight mechanics) and the elastic degrees of freedom (structural modal analysis) are combined into one decoupled set of first-order ordinary differential equations (the decoupling enabled by the mean-axis condition [32]). These equations are solved by the implicit linear multistep Adams-Moulton method [31], and their results are loosely coupled with TAU-URANS simulation. The flight mechanics module is not described in a separate section in the paper. It solves a system of 13 nonlinear first-order ordinary differential equations of unsteady translational and rotational 6DoF motion (Newton's second law) of the free-flying, rigid aircraft reacting to external loads with the reference frame at the center of gravity (CG). The RBF CFD mesh deformation is performed in every time step by sequential execution of control surface deflections, HTP rotation, and aircraft elastic deformation. More detailed information of all UltraFLoads parts, a description of individual equations, and used assumptions can be found in [18].



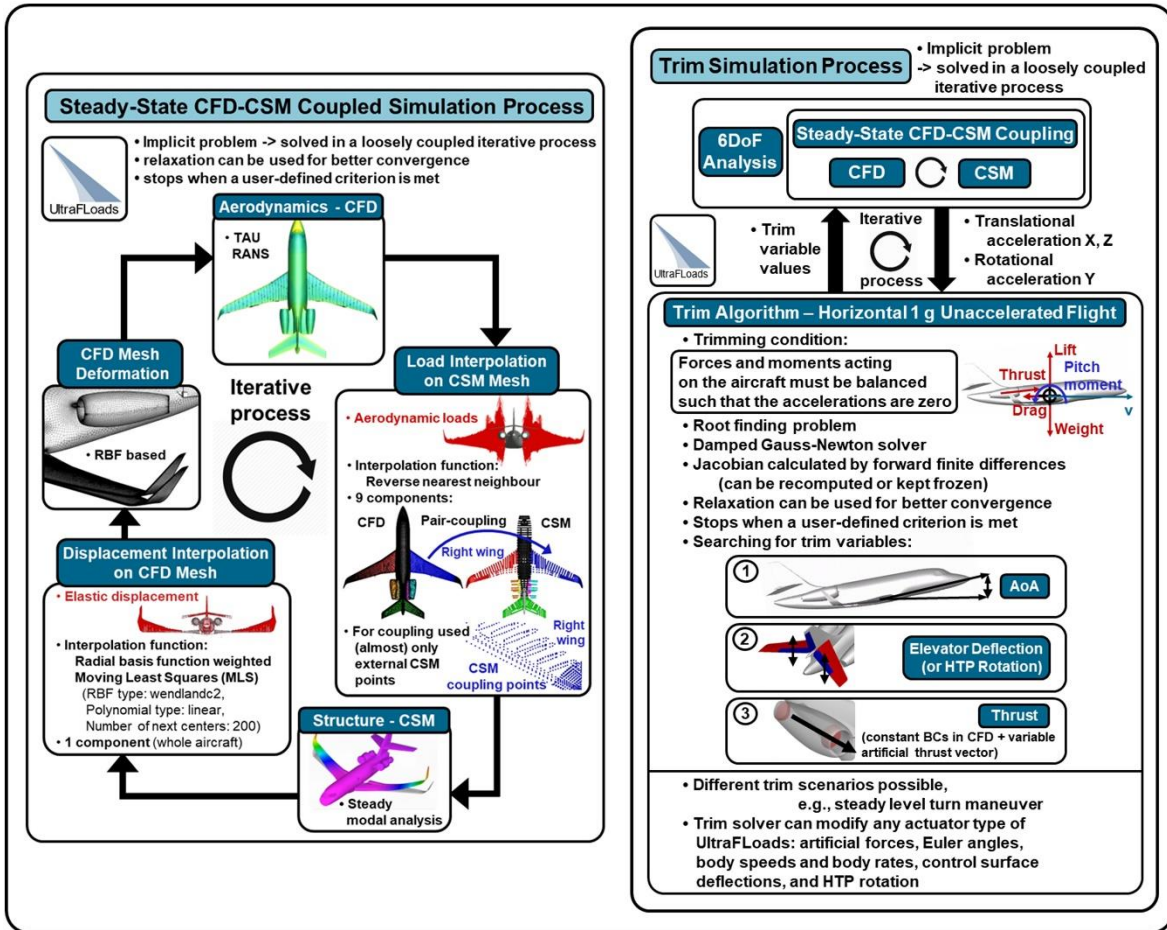


Figure 12: UFL processes of steady-state CFD-CSM coupled simulation and trim simulation.

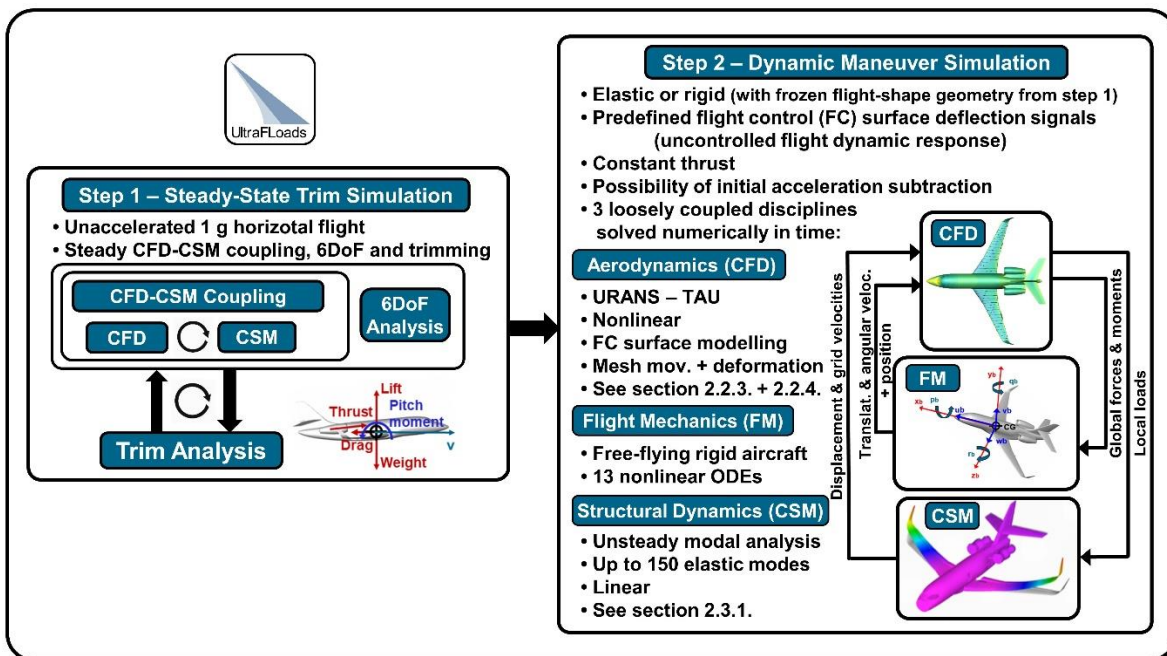


Figure 13: UFL process of dynamic maneuver simulation.

### 3 RESULTS OF ISTAR MANEUVER SIMULATIONS

The following sections present the first ISTAR maneuver simulation results and first comparisons with experimental data. These comparisons do not serve as a proper validation of numerical simulations but as an initial check of the overall simulation process functionality, numerical models, and correct parameter settings.

#### 3.1 Results – Simulations of steady-state trimmed horizontal 1 g flights

##### 3.1.1 Specific range – Comparison with the aircraft performance manual

The left part of Figure 14 depicts specific range curves of the ISTAR aircraft for different flight altitudes and speeds in cruise flight. The red curves represent data from the Falcon 2000LX performance manual [33], and the blue curves show the numerical simulation results computed with FSAerOpt (steady-state CFD-CSM, trimmed horizontal 1 g flight simulation). FSAerOpt was chosen due to its ability to couple with the DLRp2 engine model (engine specific fuel consumption is required for the specific range). The specific range of the numerical simulations (nautical miles per pound of fuel) is calculated using the Breguet range equation and a simplified thrust-drag bookkeeping in FSAerOpt [15]. The diagram in Figure 14 shows good correspondence between the numerical simulations and the official performance manual data from the manufacturer at lower flight altitudes. The deviation increases with increasing altitude, and the largest can be observed at the flight altitude of 45000 ft. It is unclear whether it is an inaccuracy from the CFD or CSM computation or the engine model (inaccurate engine model calibration for higher altitudes). A single trim simulation with CFD mesh of 18 million points in half configuration (full configuration solutions displayed in Figure 14 are mirrored) takes about 20 hours on 896 CPUs computed on the DLR-HPC cluster CARA.

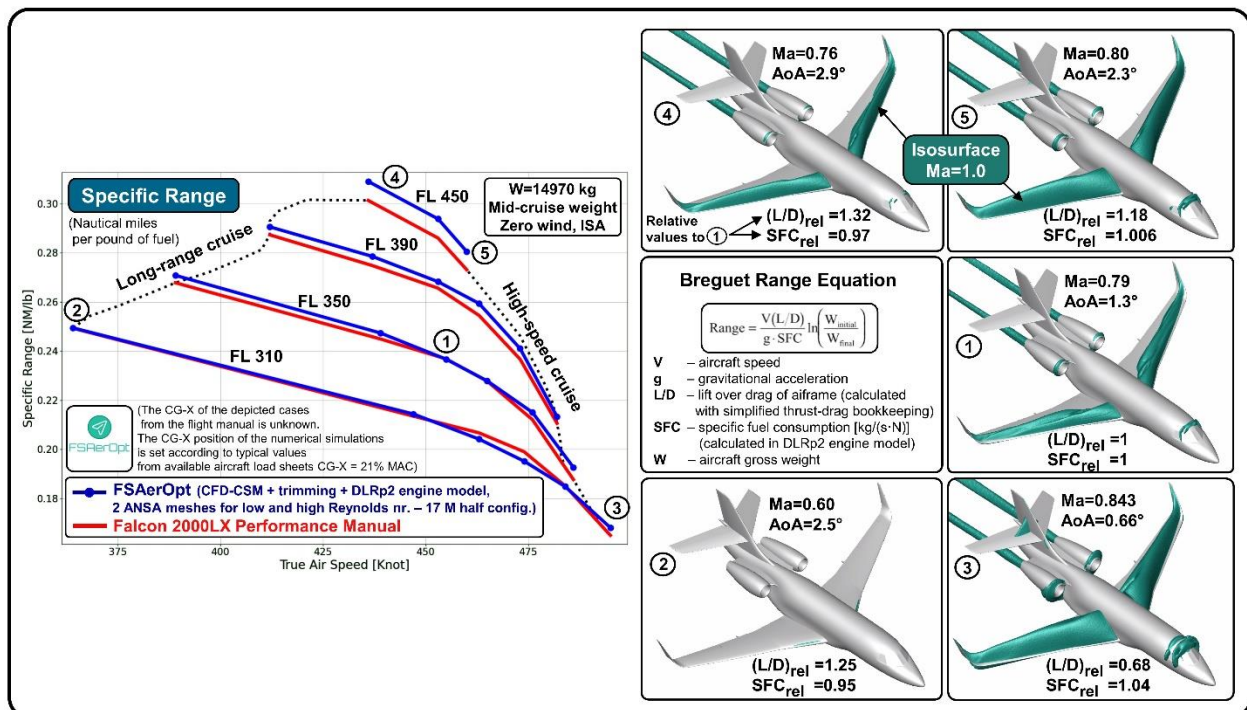


Figure 14: ISTAR specific range – comparison with aircraft performance manual.

### 3.1.2 Parameter variation study of steady-state trimmed simulation

This section describes a parameter variation study of steady-state CFD-CSM coupled trimmed horizontal 1 g simulation for one flight case (Ma=0.79, FL370 and W=13603 kg) from the HighFly measurement campaign PID (Parameter Identification). In this first HighFly flight campaign, static pressures and elastic deformations on the wing were not measured as in the flight campaign MaGE (Figure 3). Figure 15 contains four diagrams with different groups of parameter variations. The task is to compare numerical results with experimental data and conduct the first sensitivity study of different numerical parameters to trim variables. The horizontal axes represent the trim variable elevator deflection with a constant HTP rotation of  $-0.725^\circ$ , and the vertical axes represent the angle of attack (thrust is not presented). Each diagram shows the same flight measurement trim variables with a red hexagon in the upper right corner. The flight data angle of attack ( $1.3^\circ$ ) is a corrected value of the nose boom measurement (in the PID flight campaign, unlike in MaGE, the nose boom was used). The angle of attack measurement correction model has a maximum error of up to  $0.3^\circ$  and was created at the DLR Institute of Flight Systems in Braunschweig using the measurement data from the HighFly flight campaign PID [34, 35]. These correction model errors (not only for the angle of attack) must be considered when comparing experimental data with numerical results. All displayed numerical results are computed with UltraFLoads (except for one case – yellow triangle in Diagram 1). The CFD mesh type is described in the diagrams.

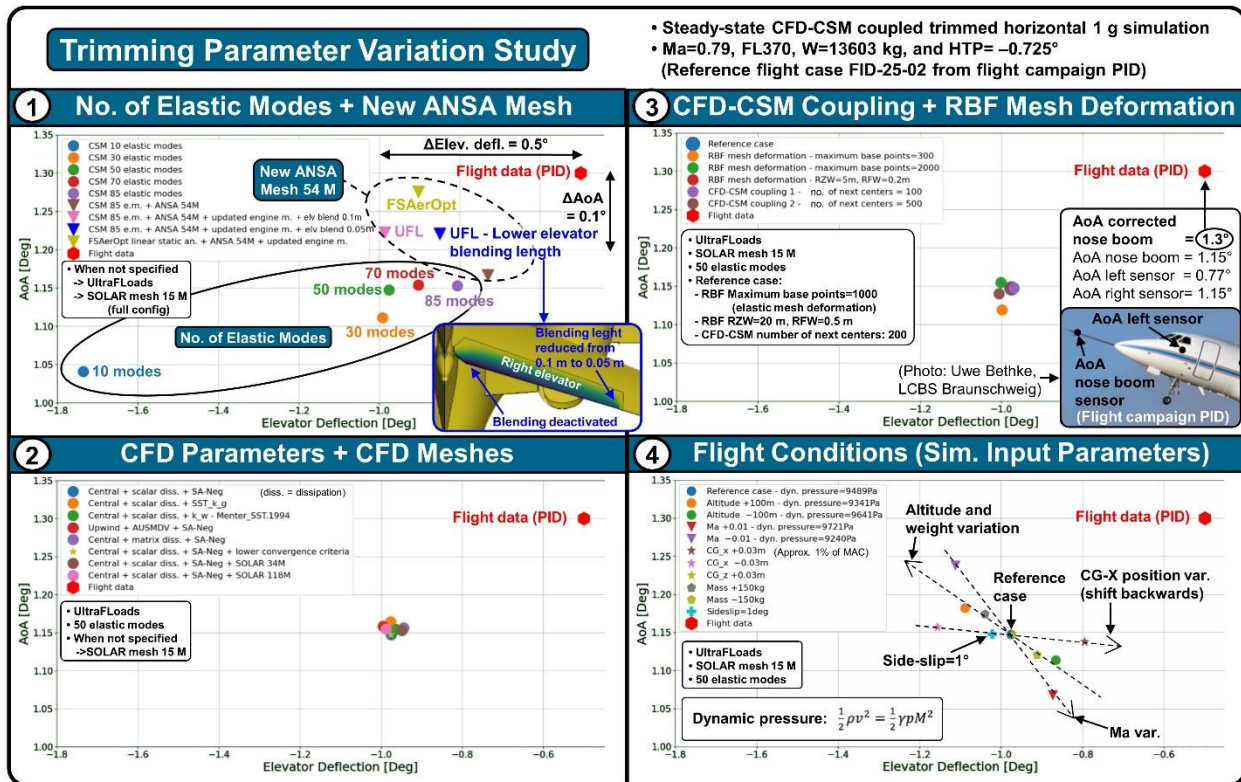


Figure 15: Parameter variation study of trimmed simulation.

Diagram 1 (Figure 15) shows the calculations with different numbers of elastic modes used in the structural modal analysis calculation (solid line ellipse). A significant sensitivity can be observed. The number of elastic modes determines the level of approximation of the elastic deformation and thus affects the aircraft flight shape in CFD and the transonic flow around it. A disadvantage when



using a high number of elastic modes in dynamic maneuver simulations is the necessity of a small simulation time step size (high number of URANS calculations) due to maximum structural frequencies. Next, the dashed line ellipse (Diagram 1) contains the latest results with a new, more refined ANSA CFD mesh (54 million points in full configuration), 85 elastic modes, and new engine boundary conditions from an updated DLRp2 engine model (pink triangle). A single FSAerOpt calculation (yellow triangle) with the linear static structural analysis (no modal analysis) is also depicted. The deviation to the flight measurement in the angle of attack for these cases is up to  $0.1^\circ$ , which lies in the accuracy range of the angle of attack measurement. A more significant difference (up to  $0.5^\circ$ ) is in the elevator deflection, where a more accurate value from the experimental measurement is expected. One of the possible reasons could be the inexact elevator deflection modelling (mesh morphing approach, section 2.2.4). Therefore, another simulation (blue triangle) with the reduced elevator blending length is calculated. Due to the higher elevator efficiency, it shows a lower negative deflection value, which is still significantly different from the experimental value. A comparison of simulations with flight control surface deflections with and without mesh morphing approach (with blending areas and with real gaps) should be performed in the future to determine the optimal blending length. Another reason in elevator deflection deviation, besides CFD, could be an inaccurate CSM model (inaccurate calculation of elastic deformation) or an inaccuracy of the center of gravity X position in the simulation, which is set according to the board computer value. The upcoming validation tasks will further investigate this higher elevator deflection deviation from the flight measurement.

Diagram 2 (Figure 15) has different TAU solver parameters such as different turbulence models, discretization schemes, and two more additional refined SOLAR meshes. Diagram 3 (Figure 15) depicts a CFD-CSM coupling and CFD mesh deformation parameter variation. Both variations in Diagram 2 and 3 evince weaker sensitivities. In flight cases with higher Mach number, higher angles of attack, higher load factor, and with flow separation, the CFD and CFD-CSM coupling parameters might show stronger sensitivities.

Diagram 4 (Figure 15) presents a variation of the simulation input parameters from measurements on the real aircraft: flight altitude, Mach number, aircraft weight, CG position, and side-slip angle. This parameter variation shows a stronger sensitivity and thus the importance of the input parameter accuracy. To correctly compare the sensitivity of these simulation input parameters with each other and with other parameters from Diagram 1-3, it is necessary to know the ranges of absolute measurement errors, which are not known for all parameters now. These results also confirm the necessity of the CG and weight measurements before and after each measurement flight for accurate validation, that were therefore carried out in the flight campaign MaGE. During the validation, considerable attention also has to be spent on CFD simulation input parameters free-stream Mach number and static pressure and their corrected experimental values. These two parameters also determine dynamic pressure, which is an essential parameter for aeroelastic calculations.



### 3.1.3 First comparison of wing pressure distributions between simulation and flight data

Figure 16 displays a first comparison of the static pressure distribution from the simulations on three wing sections DV2, DV3, and DV4 (blue curves) with the experimental static pressure from the pMEMS sensors (black dots) for two MaGE flight points (Ma=0.456 and 0.787 at the flight altitude of 25000 ft). The displayed pMEMS data, like the simulations, represent the steady-state trimmed 1 g flight. The trim variables (angle of attack and elevator deflection) are also compared in the figure. The Cp distributions of the simulations on the upper wing surface are shown on the right-hand side. Local flow effects can be observed on the pressure distributions of the individual wing sections in the areas of the beginning and end of the pMEMS belts (thickness of about 2 mm, Figure 6 and 17). This pMEMS belt effect, including the effects of other geometrical details (e.g., cables on the wing surface, Figure 17), will be described in more detail in future papers. The simulation values of the static pressure at the subsonic Mach number of 0.46 agree very well with the measured values. The largest deviations are observed at DV4, where a larger elastic deformation of the wing occurs, which is calculated iteratively in the CFD-CSM coupled simulation. Therefore, the largest differences between simulations and measurements are expected in this elastic region of the wing.

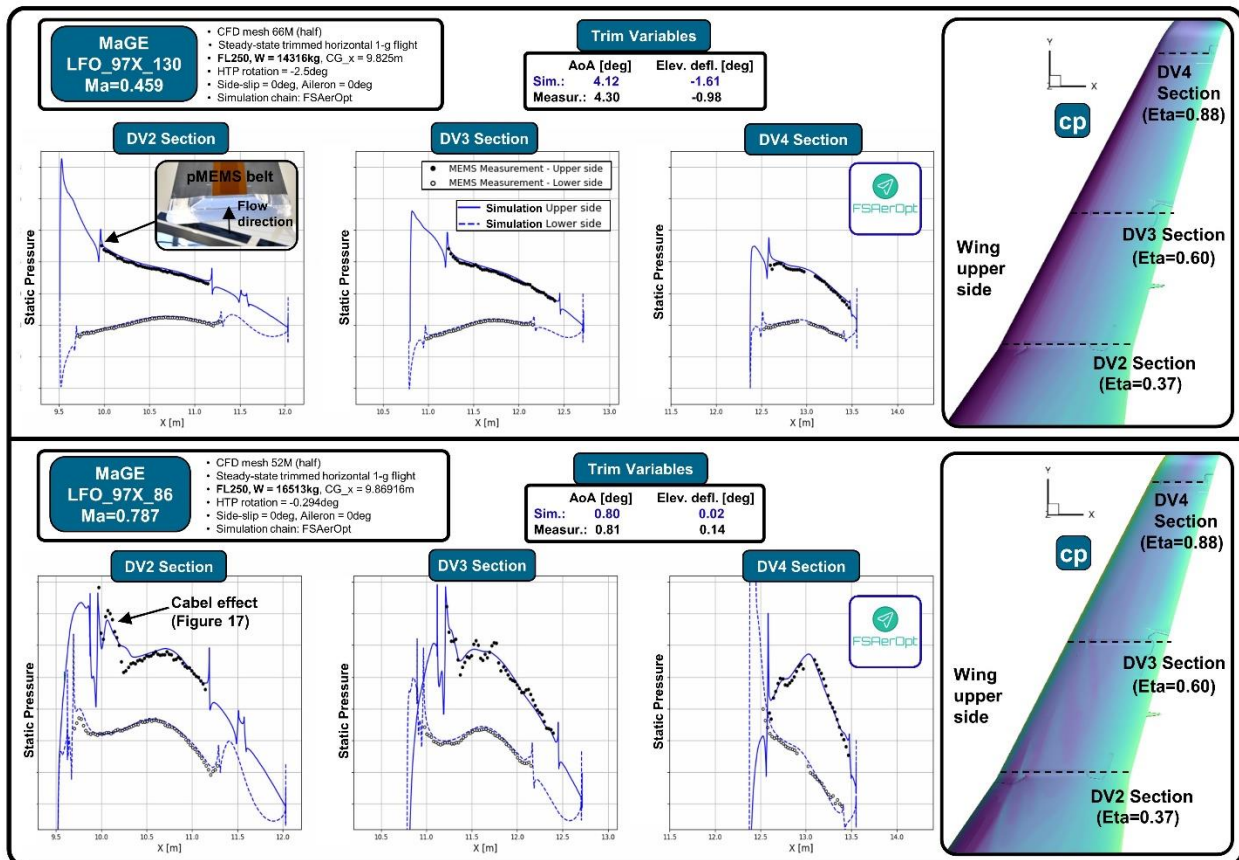


Figure 16: Static pressure on the wing - simulation vs. pMEMS measurement.

At the transonic Mach number 0.787, a relatively good agreement between the simulation and the measurement can be observed. The largest local deviations can be found on the upper side at DV2 and DV3 (zig-zag shape). There are also visible differences at DV4, which in turn could be due to an inaccurate calculation of the wing deformation.

The comparisons of pressure distributions in this chapter are only preliminary results and will be further investigated in subsequent validation activities, e.g., a study of the effect of changing various simulation parameters on the pressure distribution and the investigation of additional flight points will be performed.

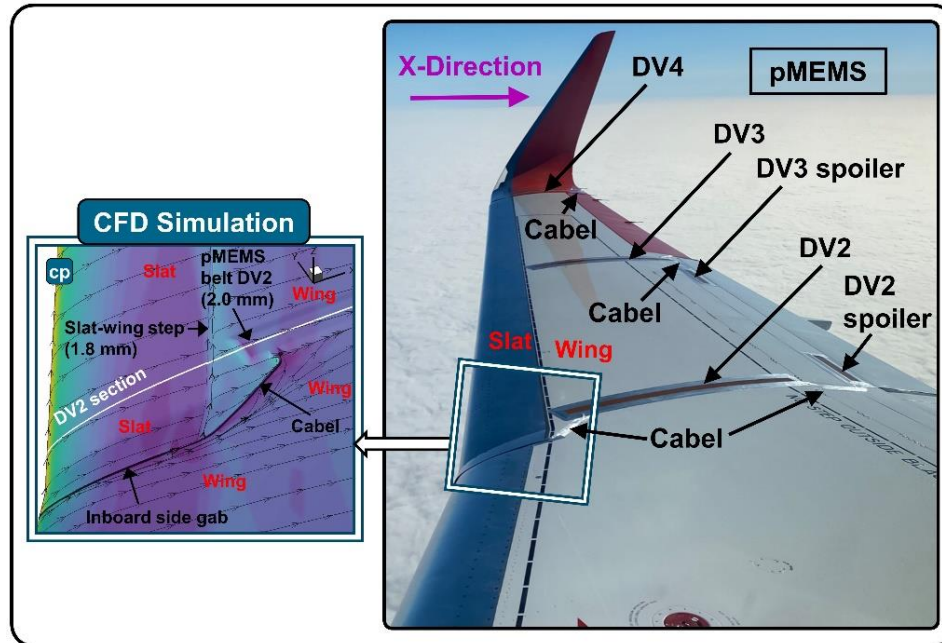


Figure 17: Geometric details of the ISTAR wing upper side from the MaGE flight campaign.

### 3.2 Results – Dynamic maneuver simulations

For the initial check of the UltraLoads dynamic maneuver simulation process with the ISTAR configuration, two maneuver types are computed: bank-to-bank and pull-up/push-down maneuver. It is an open-loop flight dynamic response of the rigid or elastic aircraft to a forced motion of the flight control surface deflection. In the first case, both ailerons are asymmetrically deflected ( $\pm 5^\circ$ ). In the second case, both elevators are symmetrically deflected ( $\pm 3.5^\circ$ ). A CFD ANSA mesh with 54 million points (full configuration), 85 elastic modes in the modal analysis, and time step size  $\Delta t = 0.003$  s are used in elastic simulations. The initial flight conditions of the trimmed unaccelerated flight are  $Ma = 0.79$ , FL370, and aircraft gross weight of 13603 kg (the same flight state as in section 3.1.2). Both maneuvers are displayed in Figure 18 with the following variables: control surface deflection signal, Euler angles (position angles), angle of attack, side-slip angle (only for the first maneuver), load factor (only for the second maneuver), and lift and pressure coefficient distributions for three selected time points of both maneuvers.

The left part of Figure 18 shows the aircraft response to an aileron deflection doublet. The rolling motion with the typical aerodynamic roll rate damping is visible. This effect can also be seen on the wing lift distribution of the time point 2. The aircraft angle of attack changes only slightly during the maneuver. The side-slip angle is more responsive due to the roll-yaw coupling (adverse yaw) and Dutch roll oscillations. The elastic simulation evinces significantly lower maximal roll angles compared to the rigid simulation, which is due to the elastic twisting effect and therefore a reduction in the efficiency of the ailerons. During the downwards aileron deflection, the flow is locally separated on the upper side of the aileron.

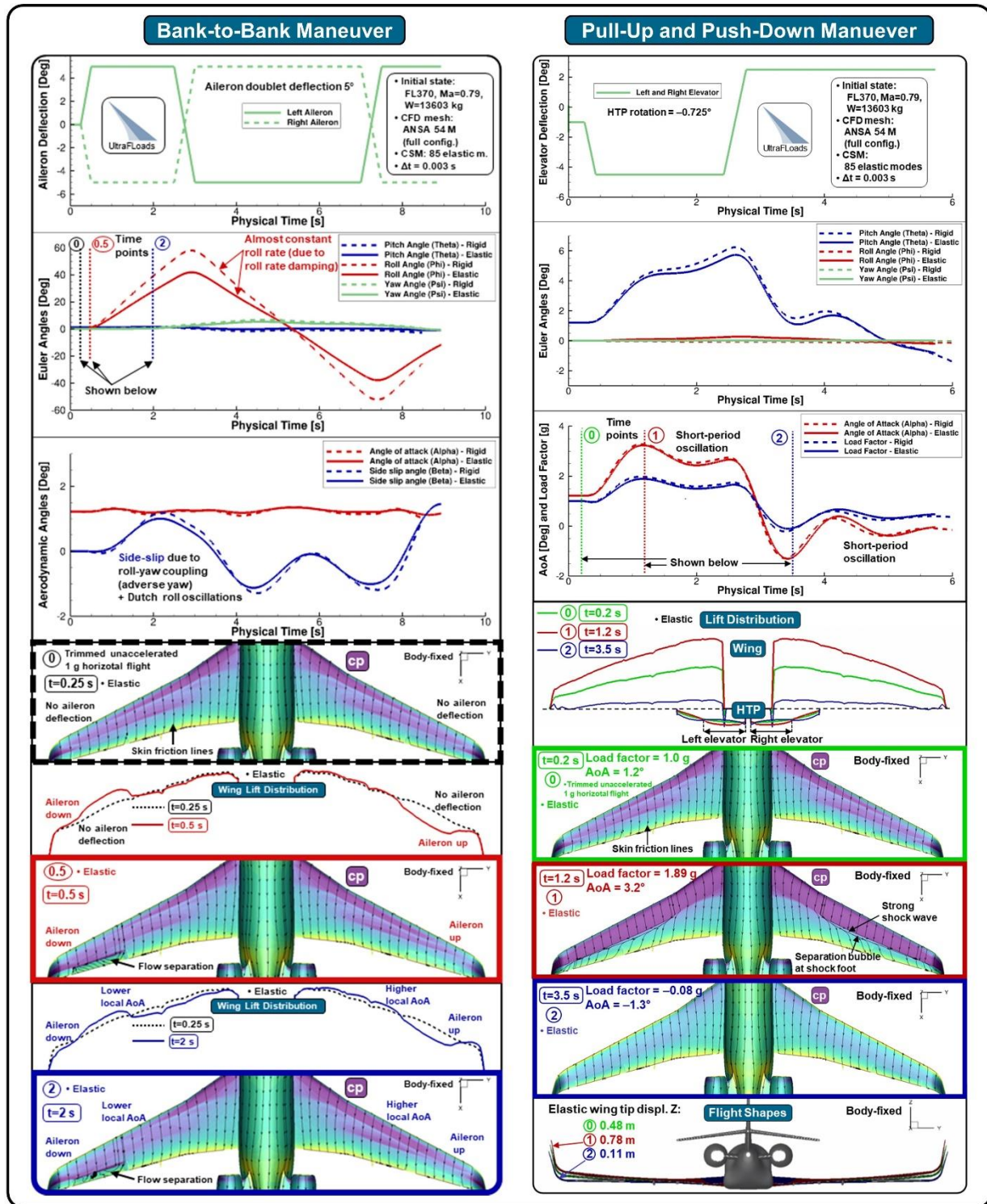


Figure 18: Bank-to-bank and pull-up and push-down maneuver simulation (UFL).



The right part of Figure 18 displays the pull-up and push-down maneuver with a significant variation of pitch angle, angle of attack, and load factor. Short-period oscillations and aerodynamic pitch rate damping visible on the HTP lift distributions can be observed. At time point 1 (1.89 g), a separation bubble at the shock foot occurs. The difference between the elastic and the rigid simulation is not as significant as in the bank-to-bank maneuver.

All presented simulations were computed on the DLR-HPC clusters CARA and CARO (Figure 19). The presented bank-to-bank maneuver simulation in Figure 18 (CFD mesh with 54 million points) with a physical time of 9 s (6080 time step iterations) took about 310 hours on 1792 CPUs on CARO (1.45 days of computation per physical second).

Figure 20 depicts another maneuver simulation with a more aggressive pull-up elevator deflection than in Figure 18. An oscillation of the shock wave and periodic separation and attaching of the flow behind the shock wave can be observed. The buffet onset value from the Falcon 2000LX flight manual [33] for the presented flight altitude, Mach number, and gross weight is also shown in the diagram (load factor=2.2 g), which agrees with the numerical simulation. The shock wave oscillation amplitude and frequency when using RANS with SA-neg (unlike shock buffet onset boundary) might differ more from reality. This will be investigated with the measurement data from the flight campaign MaGE, where a light buffet occurred during some maneuvers.

Figure 21 compares the bank-to-bank UltraFlloads maneuver simulation (only the first phase) and the flight data from the HighFly flight campaign PID. In-flight measurements were taken while manual maneuvering with the autopilot off, dampers off, and at constant thrust. During this maneuver, the elevators and rudder are also slightly deflected. The left part of the figure depicts the roll angle of the simulations with different numbers of elastic modes together with flight data values (red curve). The higher the number of elastic modes, the closer the simulation result is to the flight data. The diagram also shows a variation of aileron blending length, which influences the effectiveness of aileron deflection. The right part of Figure 21 displays only the simulation with 85 elastic modes with flight data and compares the roll angle, angle of attack, and side-slip angle. Sufficient qualitative correspondence between the simulation and measured data can be observed for this initial check (maximal deviation of roll angle  $\approx 3.5^\circ$ ).




	DLR Supercomputer CARA	DLR Supercomputer CARO
		
Top500 worldwide ranking:	494 (2022/11)	228 (2023/11)
Location:	Germany - Dresden	Germany - Göttingen
Installation year:	2019	2021
No. of cores:	145 920	174 592
Processor:	AMD Epyc 7601 32C 2.2GHz	AMD EPYC 7702 64C 2GHz
Theoretical peak (Rpeak):	2.57 PFlop/s	5.59 PFlop/s
Total storage:	17 PB	8.4 PB
Max. power consumption:	1.2 Megawatt	0.8 Megawatt

Figure 19: DLR supercomputers CARA and CARO.



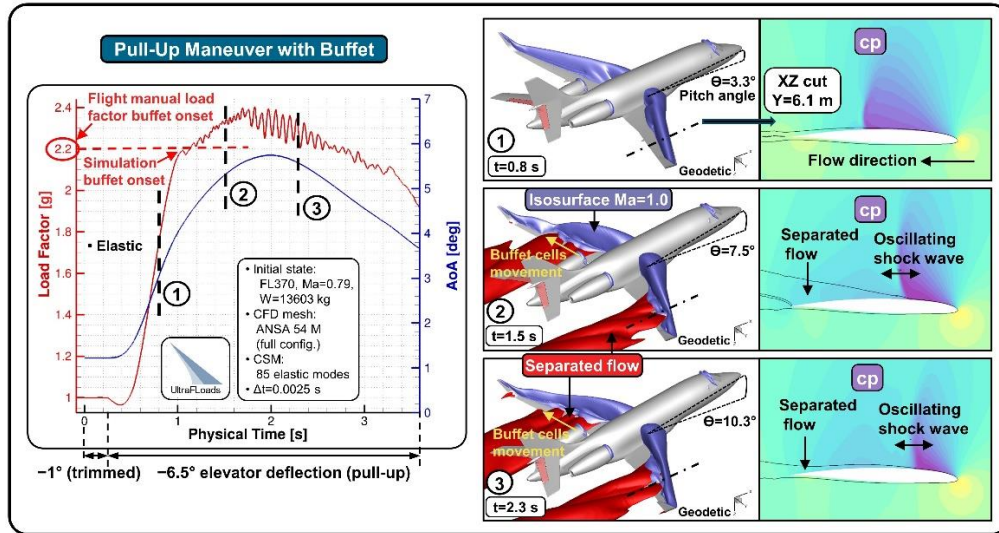


Figure 20: Pull-up maneuver simulation with buffet (UFL).

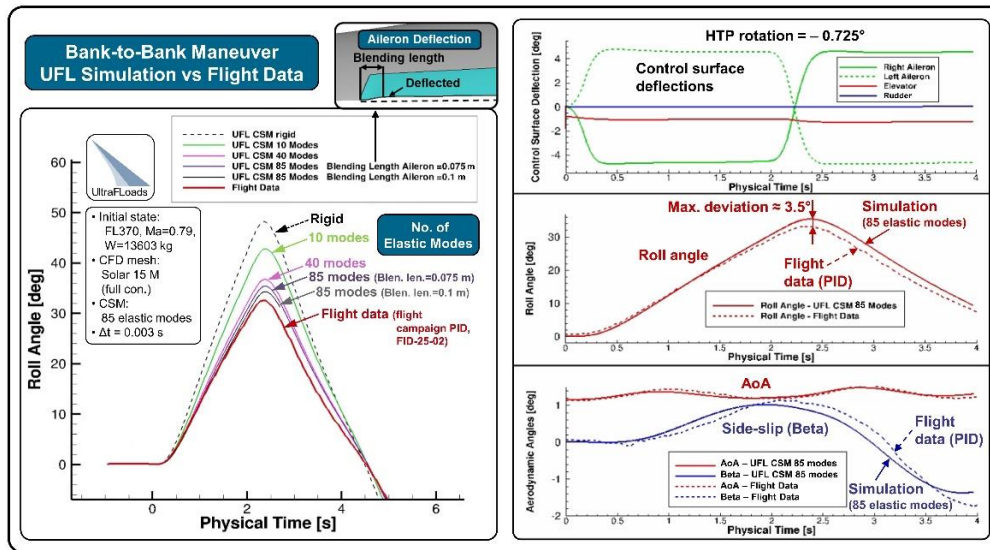


Figure 21: Bank-to-bank maneuver simulation (UFL) – comparison with flight data.

#### 4 CONCLUSION AND OUTLOOK

This paper presents numerical models and analyses of the high-fidelity multidisciplinary maneuver simulations of the DLR research aircraft Dassault Falcon 2000LX ISTAR. The first results of the trimmed steady-state and dynamic maneuver simulations of ISTAR in clean cruise configuration computed in the framework of the DLR project HighFly with the process chains FSAerOpt and UltraFLoads are displayed together with the first comparisons with experimental data. These comparisons serve as an initial check of the overall simulation process functionality and show in most cases sufficient qualitative and quantitative correspondence for this phase of the first results. Larger differences were observed only in Figure 14 (specific range) at higher flight altitudes and in Figure 15 (steady-state trimmed simulation, parameter variation study) in elevator deflection value. The calculated simulations were also used to remove the process chain deficiencies; to gain experience with process control, parameter settings, and post-processing; and to give useful

feedback to process chain developers. They are still working on implementation of new capabilities of the whole simulation process.

The computations of the ISTAR maneuver simulations (steady-state trimmed cases and dynamic maneuvers) will continue in the project HighFly and beyond in validation activities with the flight data measured in the HighFly flight campaign MaGE. Global flight mechanics parameters, wing section pressure distributions measured on three wing sections by pMEMS sensors, and elastic wing deformation distribution measured by IPCT will be compared with simulations. The results of these validations will be introduced in future papers. The deviations between numerical simulation results and flight measurements described in this paper will also be further investigated during these ongoing validation activities.

## REFERENCES

- [1] German Aerospace Center (DLR): Simulation Based Certification. <https://www.dlr.de/en/research-and-transfer/projects-and-missions/simulation-based-certification> Accessed 21 May 2024
- [2] American Institute of Aeronautics and Astronautics: Recommended Practice: When Flight Modelling Is Used to Reduce Flight Testing Supporting Aircraft Certification (AIAA R-154-2021). <https://doi.org/10.2514/4.106231>
- [3] Collar, A.R.: The Expanding Domain of Aeroelasticity. *The Journal of the Royal Aeronautical Society*. 1946,50(428):613-636. <https://doi.org/10.1017/S0368393100120358>
- [4] DLR Institute of Aerodynamics and Flow Technology: HighFly - Aerodynamics, aeroelasticity, structures and propulsion on the ISTAR research aircraft. <https://www.dlr.de/en/as/research-and-transfer/projects/highfly> Accessed 21 May 2024
- [5] German Aerospace Center (DLR): ISTAR Dassault Falcon 2000LX D-BDLR. <https://www.dlr.de/en/research-and-transfer/research-infrastructure/research-aircraft-fleet/istar-dassault-falcon-2000lx-d-bdlr> Accessed 21 May 2024
- [6] DLR: DLR conducts vibration tests on ISTAR. [https://www.dlr.de/en/latest/news/2021/03/20210702\\_vibrating-research-aircraft](https://www.dlr.de/en/latest/news/2021/03/20210702_vibrating-research-aircraft) Accessed 16 August 2023
- [7] DLR: Four hundred flight manoeuvres with ISTAR advance its digital twin. <https://www.dlr.de/en/latest/news/2023/02/four-hundred-flight-manoevres-with-istar-advance-its-digital-twin> Accessed 15 August 2023
- [8] Raab, C., Rohde-Brandenburger, K.: Dynamic flight load measurements with MEMS pressure sensors. *CEAS Aeronaut J* 12, 737–753 (2021). <https://doi.org/10.1007/s13272-021-00529-3>
- [9] German Aerospace Center (DLR): Image Pattern Correlation Technique (IPCT). <https://www.dlr.de/en/as/about-us/departments/experimental-methods/image-pattern-correlation-technique-ipct> Accessed 21 May 2024
- [10] Bauer, M., Feldwisch, J.M: High-Fidelity Multidisciplinary Maneuver Simulations of Falcon 2000LX ISTAR. In: *DLRK 2023 - Deutscher Luft- und Raumfahrtkongress*, 19-21 September 2023, Stuttgart (2023)
- [11] Meinel, M., Einarsson, G.: The FlowSimulator framework for massively parallel CFD applications. *PARA 2010* (2010)

- [12] Reimer, L., Heinrich, R., Geisbauer, S., Leicht, T., Görtz, S., Ritter, M., Krumbein, A.: Virtual Aircraft Technology Integration Platform: Ingredients for Multidisciplinary Simulation and Virtual Flight Testing. In: AIAA Scitech 2021 Forum. 11-15 & 19-21 January 2021. <https://doi.org/10.2514/6.2021-1202>
- [13] Hexagon: MSC Nastran. <https://hexagon.com/de/products/product-groups/computer-aided-engineering-software/msc-nastran> Accessed 25 August 2023
- [14] Kroll, N., Langer, S., Schwöppe, A.: The DLR Flow Solver TAU – Status and Recent Algorithmic Developments. In: 52th AIAA Aerospace Sciences Meeting (2014). <https://doi.org/10.2514/6.2014-0080>
- [15] Merle, A., Ronzheimer, A., Bekemeyer, P., Görtz, S., Keye, A., Reimer, L.: Gradient-based Optimization of a flexible long-range transport Aircraft using a high-dimensional CAD-ROM Parameterization. In: DLRK 2018 - Deutscher Luft- und Raumfahrtkongress, 04–06 September 2018, Friedrichshafen (2018)
- [16] Merle, A., Stück, A., Remke, A.: An Adjoint-based Aerodynamic Shape Optimization. In: 35th AIAA Applied Aerodynamics Conference (2017). <https://doi.org/10.2514/6.2017-3754>
- [17] Feldwisch, J.M., Reimer, L., Ritter, M.: UltraFLoads - A Framework for High-Fidelity Loads Computations. In: DLRK 2021 - Deutscher Luft- und Raumfahrtkongress, 31-02 August-September 2021, Bremen (2021)
- [18] Feldwisch, J.M., Bauer, M.: UltraFLoads: A Simulation Suite and Framework for High-Fidelity Flight Loads. *Aerospace* 2023, 10, 273. <https://doi.org/10.3390/aerospace10030273>
- [19] Feldwisch, J.M., Schulze, M.: High-Fidelity Aeroelastic Loads Calculation for a Transport Aircraft Configuration Including Pitch and Roll Maneuvers. In: Dillmann, A., Heller, G., Krämer, E., Wagner, C. (eds) *New Results in Numerical and Experimental Fluid Mechanics XIII. STAB/DGLR Symposium 2020. Notes on Numerical Fluid Mechanics and Multidisciplinary Design*, vol 151. Springer, Cham. [https://doi.org/10.1007/978-3-030-79561-0\\_50](https://doi.org/10.1007/978-3-030-79561-0_50)
- [20] Zimmer, M., Feldwisch, J.M., Ritter, M.: Coupled CFD-CSM Analyses of a Highly Flexible Transport Aircraft by Means of Geometrically Nonlinear Methods. In: 19. International Forum on Aeroelasticity and Structural Dynamics, Madrid, 13-17 Juni 2022.
- [21] Dassault Systems: Catia. <https://www.3ds.com/products-services/catia/> Accessed 25 August 2023
- [22] Martineau, D., Stokes, S., Munday, S., Jackson, A., Gribben, B.: Anisotropic Hybrid Mesh Generation for Industrial RANS Applications. AIAA-paper, AIAA Aerospace Conference, pp. 2006-534 (2006). <https://doi.org/10.2514/6.2006-534>
- [23] BETA Simulation Solution: High Fidelity Automated CFD - Advanced Modeling & Simulation Seminar Series. [https://www.nas.nasa.gov/assets/nas/pdf/ams/2021/AMS\\_20210615\\_Skaperdas.pdf](https://www.nas.nasa.gov/assets/nas/pdf/ams/2021/AMS_20210615_Skaperdas.pdf) Accessed 22 August 2023
- [24] NASA: The Spalart-Allmaras Turbulence Model. <https://turbmodels.larc.nasa.gov/spalart.html> Accessed 22 August 2023
- [25] NASA: The Menter Shear Stress Transport Turbulence Model. <https://turbmodels.larc.nasa.gov/sst.html> Accessed 25 August 2023

- [26] DLR: Technical Documentation of the DLR TAU-Code Release 2019.1.2. Page 117 (2019)
- [27] Görtz, S., Leicht, T., Couaillier, V., Méheut, M., Larrieu, P., Champagneux, S.: CODA: A European Perspective for a Next-Generation CFD, Analysis and Design Platform. In: NATO Applied Vehicle Technology (AVT) Panel (2022)
- [28] Reimer, L.: User guide of FS Ctrl Surf Displ Field Generator. DLR Institute for Aerodynamics and Flow Technology, Braunschweig (2015)
- [29] Remke, A.: User Guide FS Mesh Deformation. DLR AS-CASE, Braunschweig (2020)
- [30] Becker, R.G., Reitenbach, S., Klein, C., Otten, T., Nauroz, M., Siggel, M.: An Integrated Method for Propulsion System Conceptual Design. In: Proceedings of ASME Turbo Expo 2015: Turbine Technical Conference and Exposition. <https://doi.org/10.1115/GT2015-43251>
- [31] Hairer, E., Nørsett, S., Wanner, G.: Multistep Methods and General Linear Methods. In: Solving Ordinary Differential Equations I: Nonstiff Problems. pp. 303-432. Springer: Berlin/Hedelberg, Germany (1987). <https://doi.org/10.1007/978-3-540-78862-1>
- [32] Buttrill, C., Arbuckle, P., Zeiler, T.: Nonlinear simulation of a flexible aircraft in maneuvering flight. In: Flight Simulation Technologies Conference, Monterey, CA, U.S.A. (1987). <https://doi.org/10.2514/6.1987-2501>
- [33] Dassault Aviation: FALCON 2000EX EASy, FALCON 2000DX, FALCON 2000LX - Airplane Flight Manual. [https://downloads.regulations.gov/FAA-2013-0862-0005/attachment\\_1.pdf](https://downloads.regulations.gov/FAA-2013-0862-0005/attachment_1.pdf) Accessed 9 September 2023
- [34] Raab, C.: Dassault Falcon 2000LX ISTAR – Flight Data Gathering and DCC for System Identification – V1.00. DLR, Braunschweig (2022)
- [35] Raab, C.: Practical examples for the flight data compatibility check. CEAS Aeronaut J 14, 1019–1033 (2023). <https://doi.org/10.1007/s13272-023-00687-6>

## **COPYRIGHT STATEMENT**

The authors confirm that they, and/or their company or organisation, hold copyright on all of the original material included in this paper. The authors also confirm that they have obtained permission from the copyright holder of any third-party material included in this paper to publish it as part of their paper. The authors confirm that they give permission, or have obtained permission from the copyright holder of this paper, for the publication and public distribution of this paper as part of the IFASD 2024 proceedings or as individual off-prints from the proceedings.